

# Turbulent bifurcations in intermittent shear flows : from puffs to oblique stripes

Takahiro Ishida<sup>1</sup>, Yann Duguet<sup>2</sup>, and Takahiro Tsukahara<sup>1</sup>

<sup>1</sup>*Department of Mechanical Engineering, Tokyo University of Science, 278-8510 Chiba, Japan*

<sup>2</sup>*LIMSI-CNRS, Campus Universitaire d'Orsay, Université Paris-Saclay, 91405 Orsay, France*

(Dated: September 3, 2018)

Localised turbulent structures such as puffs or oblique stripes are building blocks of the intermittency regimes in subcritical wall-bounded shear flows. These turbulent structures are investigated in incompressible pressure-driven annular pipe flow using direct numerical simulations in long domains. For low enough radius ratio  $\eta$ , these coherent structures have a dynamics comparable to that of puffs in cylindrical pipe flow. For  $\eta$  larger than 0.5, they take the shape of helical stripes inclined with respect to the axial direction. The transition from puffs to stripes is analysed statistically by focusing on the axisymmetry properties of the associated large-scale flows. It is shown that the transition is gradual : as the azimuthal confinement relaxes, allowing for an azimuthal large-scale component, oblique stripes emerge as predicted in the planar limit. The generality of this transition mechanism is discussed in the context of subcritical shear flows.

## 1. INTRODUCTION

Subcritical wall-bounded shear flows have the ability to sustain turbulent motion despite the linear stability of the laminar regime. As the flow rate is decreased starting from the fully turbulent regime, partial relaminarisation is frequently observed prior to global relaminarisation, leading to the intermittent occurrence of turbulence in an otherwise laminar flow [1]. For cylindrical pipe flow driven by either a fixed pressure gradient or a fixed mass flux, this intermittency manifests itself as disordered sequences of so-called puffs, i.e. turbulent structures filling the cross-section of the pipe but localised in the streamwise direction [2]. The self-organisation of these trains of puffs near criticality results from the interplay between local relaminarisation events and spatial proliferation [3, 4]. For planar shear flows such as plane Couette or plane Poiseuille flow, or any combination of both [5], intermittency manifests usually itself as spatially periodic patterns of laminar-turbulent coexistence in the form of stripes of turbulence [6, 7]. These stripes display a non-zero angle with respect to the streamwise direction. Closer to the onset of turbulence, these oblique structures have been reported to break up into disjoint finite-sized turbulent spots whose interaction raises interesting questions from a phase transition point of view [8, 9]. Despite recent progress coming mainly from low-order models [1, 10], a general explanation for these different types of self-organisation is still lacking.

Identifying the conditions that lead either to puff-like or stripe-like structures in a given flow geometry would help to unravel the mechanisms responsible for the localisation of turbulence. This ambitious task suggests that a flow case should be selected with a free parameter able to bridge as continuously as possible the two limiting cases of turbulent puffs, on one hand, and turbulent stripes on the other hand. In the context of pressure-driven flows, annular Poiseuille flow (aPf) is an interesting candidate for such a homotopy procedure. This geometry features two long (ideally infinite) co-axial pipes of different radii  $R_i$  and  $R_o$  ( $> R_i$ ), between which an incompressible flow is maintained using a fixed axial pressure gradient. This flow geometry is relevant in many important industrial processes ranging from nuclear plants to heat exchangers. As in all pressure-driven flows, the dramatic drop in flow rate associated with the laminar-turbulent transition makes the issues of whether and how turbulence maintains itself important for practical situations. The shape of the associated laminar flow profile depends only on the radius ratio  $\eta = R_i/R_o$ . This profile turns out to be linearly stable even for values of the Reynolds number far above those where turbulence starts to be sustained, making the transition in this flow case clearly subcritical for all values of  $\eta$  [11, 12]. In a former paper [13], the zoology of the different manifestations of laminar-turbulent coexistence was addressed using numerical simulation in moderately long (axially periodic) domains : while helical stripe patterns dominate the low- $Re$  range for  $\eta \geq 0.5$ , only statistically-axisymmetric turbulent structures were identified for  $\eta = 0.1$  and low enough Reynolds number. The former type corresponds to the stripes found in plane Poiseuille flow (pPf) in the presence of a wall curvature that vanishes asymptotically as  $\eta \rightarrow 1^-$ . The latter type can be assimilated to puffs as in circular pipe flow, except that the presence of the inner rod implies a different velocity profile both in the laminar and turbulent zones. Simulations for intermediate  $\eta = 0.3$  featured new axially localised helical structures baptised ‘helical puffs’.

In the present numerical study, we consider all these intermittent regimes in numerical domains longer than in previous studies, parametrised as before by the radius ratio  $\eta$  with emphasis on the patterning property of localized turbulence. Another important control parameter is the Reynolds number  $Re_\tau = u_\tau d/(2\nu)$ , where  $u_\tau = \sqrt{\tau/\rho}$  is the friction velocity, with  $\tau$  the mean total wall friction proportional to the pressure gradient and  $\rho$  is the density of fluid,  $\nu$  its kinematic viscosity, and  $d = R_o - R_i > 0$  measures the spacing between the two cylinders. The details of the numerics are given in Section 2. The dynamics of the flow at marginally low values of  $Re_\tau$  is analysed in Section 3 for various values of  $\eta$  from 0.1 to 0.5. In Section 4, a statistical analysis of the transition from puffs to stripes as  $\eta$  increases is suggested, based on the statistical quantification of the large-scale flows present at the laminar-turbulent interfaces. Eventually, the generality of the transition mechanism advanced in Section 4 is discussed in Section 5.

## 2. NUMERICAL SIMULATION

The geometry is best described using the classical cylindrical coordinate system  $(r, \theta, x)$ , where the  $x$ -axis is the axis common to both cylinders. We also define the rescaled azimuthal coordinate  $z = r\theta$  and the wall-normal distance from the inner wall  $y = r - R_i$ . At  $r = R_o$  we have  $y = d$  and an azimuthal extent  $L_{z_o} = 2\pi R_o$ , while for  $r = R_i$  we have  $y = 0$  and  $L_{z_i} = 2\pi R_i$ . The specific values of  $L_{z_o}$  and  $L_{z_i}$  are listed in Table I. Periodicity is considered in both  $x$  and  $\theta$ , with respective spatial periods  $L_x$  and  $2\pi$ , while no slip ( $\mathbf{u} = 0$ ) is imposed at each wall. The flow between

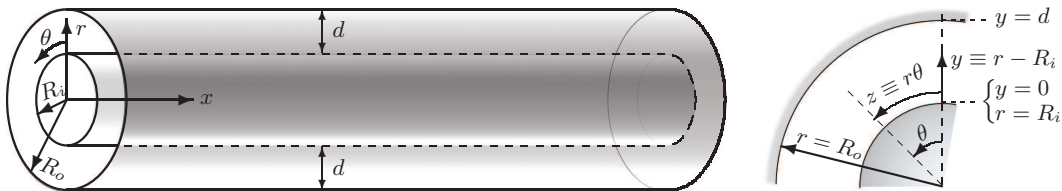


FIG. 1. Configuration of annular Poiseuille flow and coordinate system.

TABLE I. Computational conditions for DNS:  $L_x$  and  $L_z$  are the streamwise and azimuthal lengths ( $L_{zi} = 2\pi R_i$  and  $L_{zo} = 2\pi R_o$ );  $N_x$  and  $N_z$  the corresponding grid numbers ( $z = r\theta$ ), while  $N_y$  is fixed at 128 for all the cases ( $y = r - R_i$ ). Basically, longer  $L_x$  with larger  $N_x$  were used for DNS at lower  $Re_\tau$ .

$\eta$	0.1	0.2	0.3	0.4	0.5	0.8
$Re_\tau$	46–150	50–150	50–150	52–80	52–150	52–150
$L_x/d$	51.2–180.0	102.4–166.0	51.2–160.0	102.4–160.0	51.2–80.0	51.2–80.0
$L_{zi}(\eta)/d$	0.70	1.57	2.69	4.19	6.28	25.1
$L_{zo}(\eta)/d$	6.98	7.85	8.98	10.5	12.6	31.4
$N_x$	2048 or 4096	4096	2048 or 4096	4096	2048	2048
$N_z$	256	256	512	512	512	1024

the two cylinders is governed by the incompressible Navier-Stokes equations

$$\nabla \cdot \mathbf{u} = 0, \quad (1)$$

$$\partial_t \mathbf{u} + (\mathbf{u} \cdot \nabla) \mathbf{u} = -\rho^{-1} \nabla p + \nu \nabla^2 \mathbf{u}. \quad (2)$$

Denoting respectively by  $\tau_i$  and  $\tau_o$  the wall shear rate at the inner and outer wall, the axial pressure gradient at equilibrium reads  $d\bar{p}/dx = -(2/d)(\tau_o + \eta\tau_i)/(1 + \eta)$ , from which  $u_\tau = \sqrt{-\rho^{-1}d\bar{p}/dx}$  and hence  $Re_\tau$  are defined. The numerical algorithm used to solve Eqs. (1) and (2) combines fourth-order finite differences in both  $x$  and  $\theta$ , together with a second-order scheme in  $r$  on a non-uniform radial grid. Timestepping is performed using an Adams-Bashforth scheme for the nonlinear terms and a Crank-Nicolson scheme for the wall-normal viscous term, which results in a second-order algorithm. Further information about the numerical method employed here can be found in Refs. [13, 14].

All numerical parameters are reported in Table I. The local numerical resolution has been checked in our previous article [13]. The length of the computational domain has been varied between  $51d$  and  $180d$  depending on the outcome of the simulations. It is longer than most simulations from Ref. [13] in order to capture the interaction between several distinct localised turbulent structures.

### 3. TEMPORAL DYNAMICS OF LOCALISED TURBULENT STRUCTURES

The procedure (quenching from the turbulent regime) chosen here is similar to that in Refs. [13, 15]: for each value of  $\eta$ , a statistically steady turbulent flow is first reached easily by adding a random perturbation of finite amplitude to the laminar base flow at  $Re_\tau = 150$ . For this value of  $Re_\tau$ , turbulence unambiguously occupies the whole numerical domain. Then,  $Re_\tau$  is decreased in finite steps until statistically steady laminar-turbulent coexistence is detected from visualisations, usually around  $Re_\tau \approx 80$ . The control parameter is then lowered further in smaller steps until turbulence globally collapses, typically for  $Re_\tau \lesssim 50$ . Let us denote by  $Re_\tau^c = Re_\tau^c(\eta)$  the critical value of  $Re_\tau$  below which no turbulence is sustained in the long time limit. Throughout this paper, the superscript  $(\cdot)^c$  will be used to represent a critical point for sustainment of localized turbulence. However, the values suggested in this paper are not based on a full but costly statistical analysis—like e.g. in Ref. [3]—but are estimated from our limited set of simulations. We describe below the different types of spatio-temporal dynamics encountered around  $Re_\tau^c$  in order of increasing  $\eta$ . Note again that all simulations have been performed here in longer domains than in Ref. [13] and that the spatiotemporal regimes resulting from the interaction between different localised patches of turbulence are

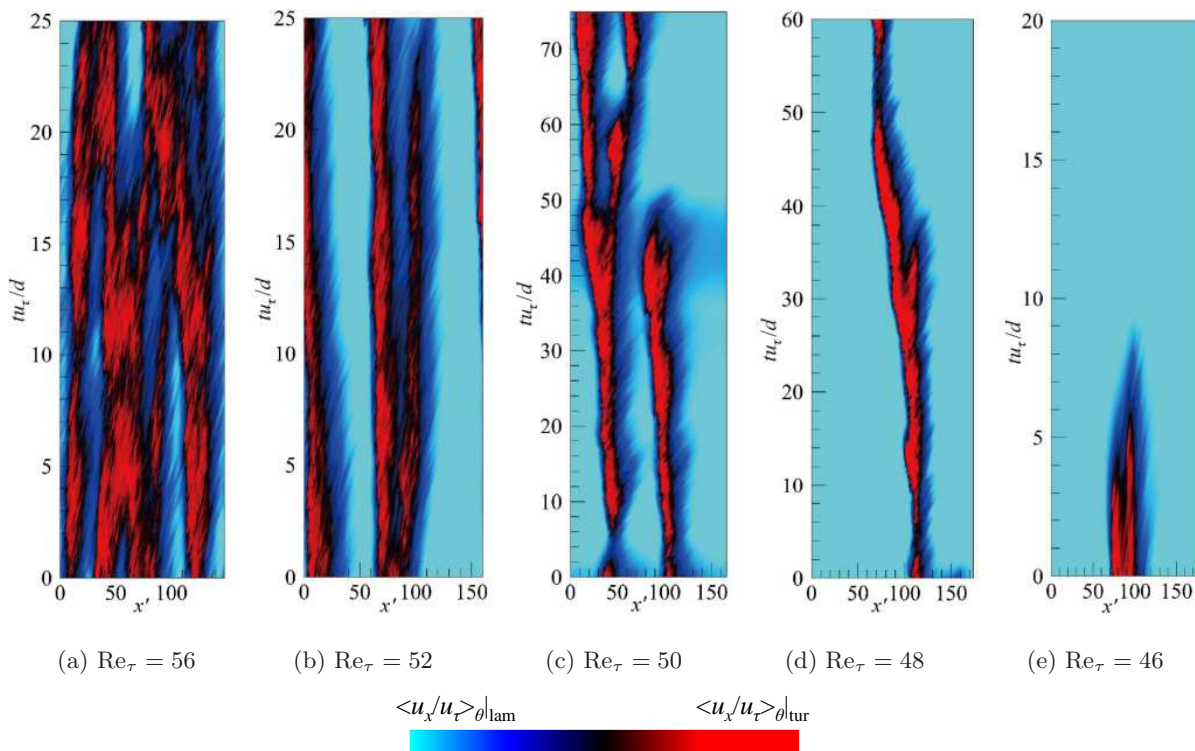


FIG. 2. Space-time diagram of azimuthally-averaged streamwise velocity at mid-gap for  $\eta = 0.1$  and different  $\text{Re}_\tau$ . Colormap of  $\langle u_x/u_\tau \rangle_\theta$  is plotted against a reduced variable  $x' = (x - ct)/d$ , in a moving frame of reference, and its range is  $(\langle u_x/u_\tau \rangle_\theta|_{\text{tur}}, \langle u_x/u_\tau \rangle_\theta|_{\text{lam}})$ : (a) (18, 22), (b) (19, 24), (c) (20, 25), (d) (21, 25), and (e) (21, 25).

more complex than in previous works. All the spatiotemporal diagrams shown in this section involve the streamwise velocity averaged azimuthally  $\langle u_x/u_\tau \rangle_\theta = \int_0^{2\pi} u_x d\theta/2\pi$ , evaluated at mid-gap.

### 3.1 Localised puffs for $\eta = 0.1$

We describe first the regimes found for low  $\eta = 0.1$ . Laminar-turbulent coexistence is easily visualised using spatiotemporal diagrams of the quantity  $\langle u_x/u_\tau \rangle_\theta$  at mid-gap as a function of the streamwise coordinate  $x$  and of the time  $t$  in units of  $d/u_\tau$ . For easier visualisation, the reduced streamwise coordinate  $x'$  is used instead of  $x$ , where  $x' = (x - ct)/d$  with  $c$  an adjustable streamwise speed. This speed of the reference frame was adjusted simply by eye in order to cancel out the apparent drift of puffs. It should be noted that the present  $c$  does not rigorously correspond to the propagation speed of puffs. Figures 2(a-e) show such diagrams for  $\text{Re}_\tau = 56, 52, 50, 48$  and  $46$ , respectively, with the colourmap adjusted so that the red colour is an indicator of local turbulent motion. For  $\text{Re}_\tau = 56$ , the flow consists of a train of four to five several puffs interacting via sequences of replication and merging events. At  $\text{Re}_\tau = 52$  and  $50$ , the number of puffs interacting drops to two or three, with relaminarisation or replication (“splitting”) events occurring on longer timescales and no merging event. For  $\text{Re}_\tau = 48$ , a single isolated puff survives over the whole observation time, though at several occasions its internal fluctuations bring it close to splitting or to collapsing. For  $\text{Re}_\tau = 46$ , the isolated puff attempts to split into two parts that both collapse after less than  $5d/u_\tau$ . This description is completely consistent with that of turbulent puffs in circular pipe flow in Refs. [3, 16, 17]. This suggests, though it remains to be properly shown, that the transition in an infinitely long pipe would be continuous, with the critical point  $\text{Re}_\tau^c$  for this value of  $\eta$  lying around  $48 \pm 1$ .

Detailed visualisation of the flow structures is achieved using the spatial fluctuations of the radial velocity  $u'_r$  around

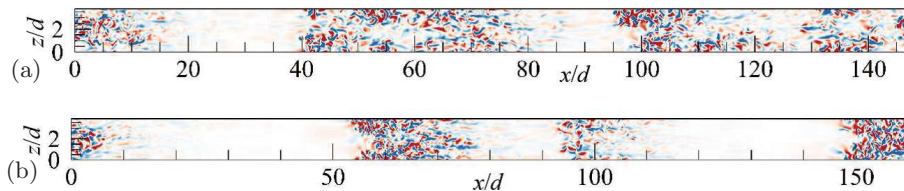


FIG. 3. Two-dimensional contours of instantaneous  $u'_r$  (blue, red)  $= (-0.75, 0.75)$  at mid-gap, for  $\eta = 0.1$  at  $\text{Re}_\tau =$  (a) 56 and (b) 52. The mean-flow direction is from left to right.

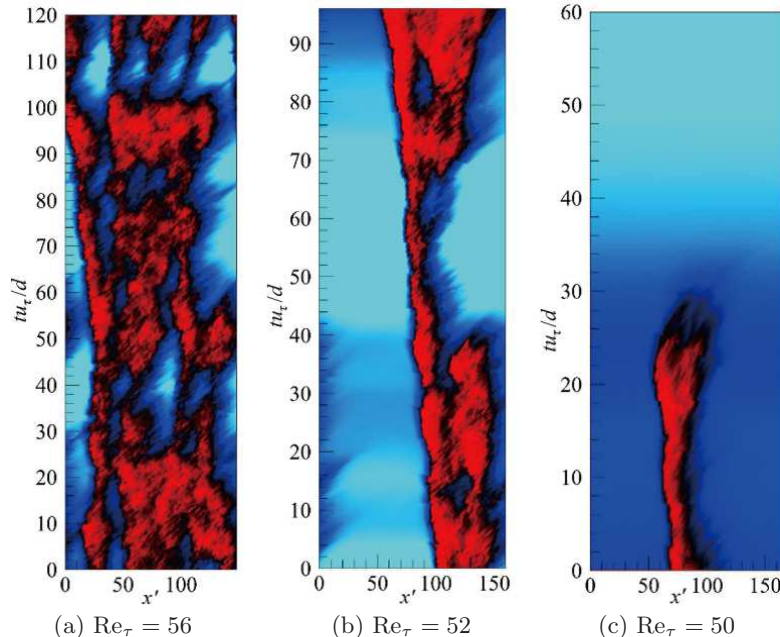


FIG. 4. Same as Fig. 2, but for  $\eta = 0.2$  :  $(\langle u_x/u_\tau \rangle_\theta|_{\text{tur}}, \langle u_x/u_\tau \rangle_\theta|_{\text{lam}}) =$  (a) (18, 23), (b) (20, 25), and (c) (20, 27).

its spatial average in a cylinder at arbitrary  $y$ . The fluctuating component is defined as :

$$u'_i = u_i - \tilde{u}_i(r, t), \quad (3)$$

$$\tilde{u}_i(r, t) = \frac{1}{L_x \cdot 2\pi} \iint u_i(x, r, \theta, t) dx d\theta. \quad (4)$$

Note that  $\tilde{u}_i$  does not necessarily equal the laminar flow, because of the presence of fully/localized turbulent region in our case—in particular, an oblique turbulent region is also accompanied by a large-scale flow also in the azimuthal direction, which may provide non-zero  $\tilde{u}_\theta$  [13]. The flow structures for  $\text{Re}_\tau = 56$  and 52 are visualised in Fig. 3. These figures confirm the resemblance with puffs from circular pipe flow (see e.g. Ref. [17] for similar visualisations of puffs close to the onset of puff splitting). In particular, each patch of turbulent fluctuations extends over the full cross-section, i.e., they are rather homogeneous in the  $z$  direction with straight laminar-turbulent interfaces.

### 3.2 Occurrence of helical puffs for $\eta = 0.2$ and 0.3

Visualisations of the intermittent flow structures and their temporal dynamics for  $\eta = 0.2$  are shown in Figs. 4 and 5 using the same quantities as in Figs. 2 and 3. The spatiotemporal diagrams for  $\text{Re}_\tau = 56$ , 52, and 50 in Fig. 4(a-c) do not differ much from those for  $\eta = 0.1$ , except perhaps at  $\text{Re}_\tau = 56$  where the turbulent flow exhibits a stronger tendency toward patterning (emergence of a well-defined streamwise wavelenght) than for lower  $\eta$ . For  $\eta = 0.2$ , the puff sustaining at  $\text{Re}_\tau = 52$  may split and avoid collapse, while the puff at  $\text{Re}_\tau = 50$  decays completely, see Figs. 4(b) and (c). This suggests a critical point around  $\text{Re}_\tau^c = 51 \pm 1$ . The spatial fluctuations of  $u'_r(x, z)$  at mid-gap in Fig. 5 show a surprising property : some of the laminar-turbulent interfaces identified display obliqueness with respect to the streamwise direction while other do not.

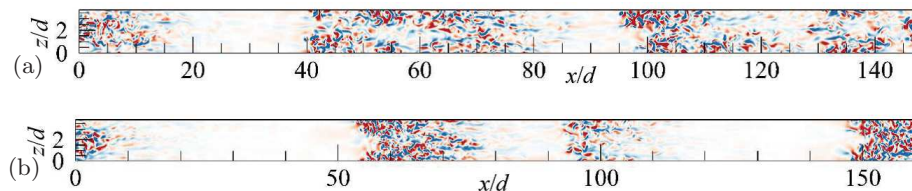


FIG. 5. Same as Fig. 3, but for  $\eta = 0.2$  at  $\text{Re}_\tau =$  (a) 56 and (b) 52.

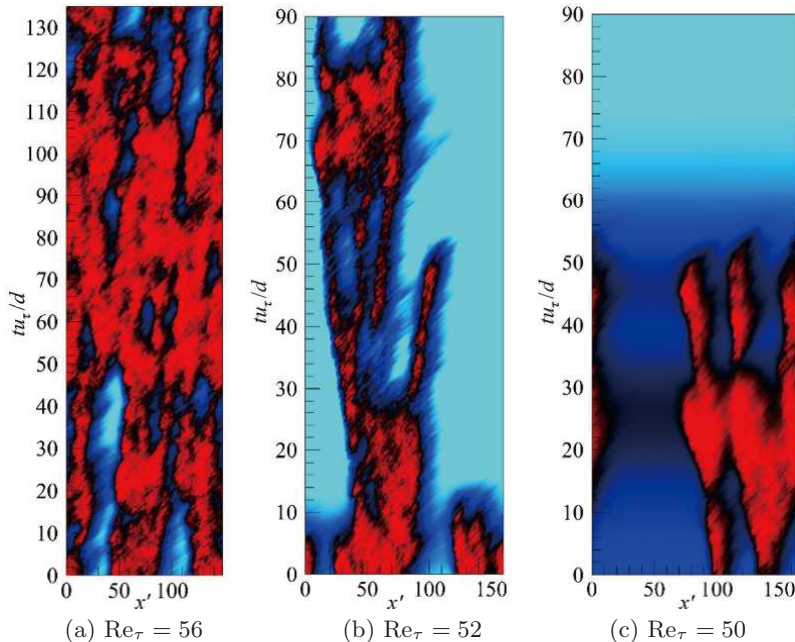


FIG. 6. Same as Fig. 2, but for  $\eta = 0.3$  :  $(\langle u_x/u_\tau \rangle_\theta|_{\text{tur}}, \langle u_x/u_\tau \rangle_\theta|_{\text{lam}}) =$  (a) (18, 22), (b) (19, 23), and (c) (19, 26).

Similar data for  $\eta = 0.3$  confirms the above-mentioned trends, with an even stronger patterning property and a comparable critical value : Fig. 6(c) provides a specific evidence that, for  $\text{Re}_\tau = 50$ , three puffs separated by a comparable wavelength collapse in synchrony. The occurrence of oblique laminar-turbulent interfaces appears also more pronounced, judging from the fluctuations of  $u'_\tau$  shown in Fig. 7. The resulting intermittent regime for  $\eta = 0.2$  and  $0.3$  appears hence as a mixture of both classical straight puffs analogous to those found for  $\eta = 0.1$ , and helical puffs as identified in Ref. [13] in shorter domains. We emphasize the coexistence in space as in time and for a given set of parameters, of both types of structures. This immediately suggests that the transition from (straight) puffs to (oblique/helical) stripes cannot be treated as deterministic, but rather requires a statistical treatment. The statistical analysis to be presented in Section 4.3 will be based on the probability density function of large-scale azimuthal velocities that is related to the obliqueness of the pattern.

### 3.3 Occurrence of stripe patterns for $\eta \geq 0.4$

Finally, the same indicators have been computed for  $\eta = 0.4$  and  $0.5$  at  $\text{Re}_\tau = 56$  and  $52$ , both apparently above the corresponding value of  $\text{Re}_\tau^c$ . The associated spatiotemporal diagrams demonstrate sustained patterning and are not shown. The spatial fluctuations shown for randomly chosen snapshots in Figs. 8 and 9 show exclusively oblique laminar-turbulent interfaces for  $\text{Re}_\tau = 56$  and apparently no puff-like structures, suggesting that this corresponds to the periodic stripe regime. In contrast,  $\text{Re}_\tau = 52$  shows a sequence of isolated spots less like a periodic pattern. A similar dynamics was reported in planar cases ( $\eta \rightarrow 1$ ) where for marginally low values of  $\text{Re}_\tau$  the stripe patterns break up into smaller structures [18], and this is a feature specific to the turbulent regimes slightly above  $\text{Re}_\tau^c$ .

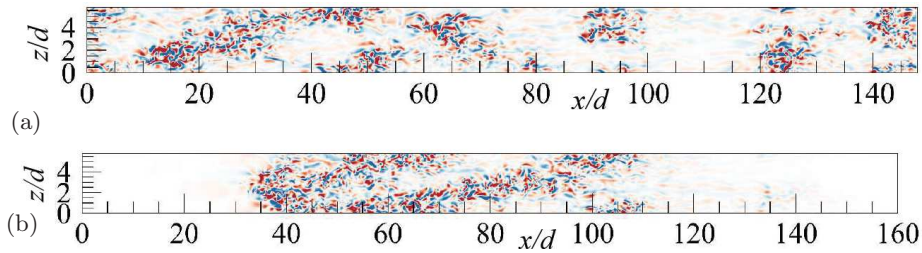


FIG. 7. Same as Fig. 3, but for  $\eta = 0.3$  at  $\text{Re}_\tau =$  (a) 56 and (b) 52.

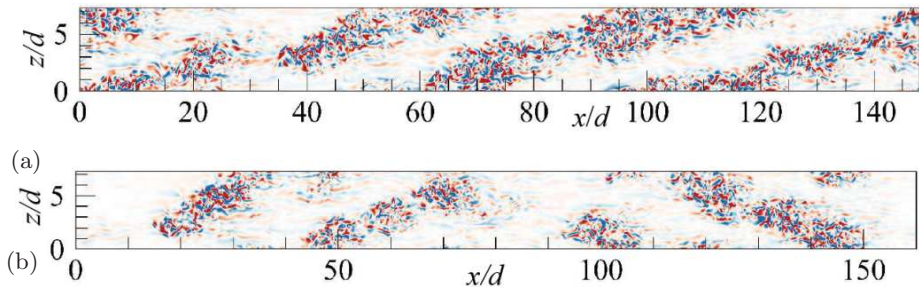


FIG. 8. Same as Fig. 3, but for  $\eta = 0.4$  at  $\text{Re}_\tau =$  (a) 56 and (b) 52.

#### 4. BIFURCATION ANALYSIS BASED ON LARGE-SCALE FLOWS

Bifurcations from one turbulent regime to another one are difficult to investigate because, unlike bifurcations of exact steady/periodic states, the presence of turbulent fluctuations both in time and space makes the choice of a well-defined bifurcation parameter non obvious. We intend here to characterise the bifurcation of the shape of coherent structures, where no particularly obvious Eulerian indicator emerges to describe for instance the obliqueness of the interfaces. We suggest to link the present study to the limiting planar case  $\eta \rightarrow 1$ , which has been already discussed in Ref. [19], and to generalise it to curved geometries corresponding to  $0 < \eta < 1$ . This represents an opportunity to test the limitations of the planar theory in the presence of finite curvature. In addition, we keep in mind the observation that both types of structures, straight and helical, have been detected for the same parameters at intermediate values of  $\eta$ . The relevant bifurcation parameter chosen should hence be quantified in a probabilistic manner, with statistics carried out, for each set of parameters  $\eta$  and  $\text{Re}_\tau$ , over both time and space.

##### 4.1 Role of the large-scale flows

For planar flows, it was suggested in Ref. [19] that the obliqueness of interfaces could be explained qualitatively by the existence of large-scale flows. In the presence of a sufficiently marked scale separation between small scales (the turbulent fluctuations) and large scales, it was shown analytically that large scales advect the small scales of weakest amplitude. Interfaces between laminar and turbulent motion correspond precisely to the zones where the fluctuations decay from their turbulent amplitude towards zero. It is thus expected that the planar orientation of the interface corresponds precisely to the orientation of the large-scale flow advecting the small scales at the edges of the turbulent patches. In particular the global angle of the periodic stripe patterns corresponds accurately to the angle of the large-scale flow (cf Fig. 2c in Ref. [19]) : a non-zero angle is linked with the existence of a spanwise component for the large scales. The small scales of interest consist essentially of streaks and streamwise vortices of finite length, which form the minimal ingredients of the self-sustaining process in all wall-bounded shear flows [20]. The origin of the transverse large scale flow is kinematic rather than dynamic : it can be derived from the mass conservation at the interfaces once streamwise localisation is assumed. In particular the role of the spanwise large-scale component in the planar case is to compensate for the loss of streamwise flow rate inside the turbulent patch (with respect to the reference flow rate inside the laminar zones).

We begin by defining the relevant quantities with notation adapted to the present cylindrical geometries for any value of  $\eta$ . Independently of temporal considerations, large-scale flows  $\mathbf{U}(x, r, \theta)$  can be obtained from any flow field

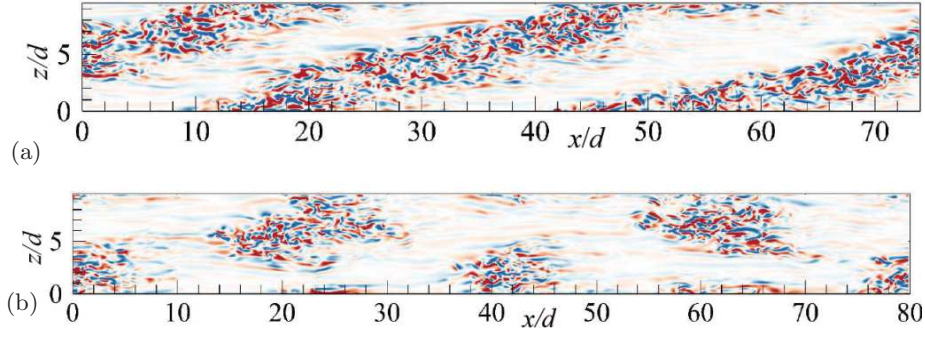


FIG. 9. Same as Fig. 3, but for  $\eta = 0.5$  at  $\text{Re}_\tau =$  (a) 56 and (b) 52.

$\mathbf{u}(x, r, \theta)$  by the application of a low-pass filter  $\mathcal{L}$  that selects only the lowest-order modes in  $\theta$  and  $x$  directions. The spectral cut-off criterion in these two directions is an intrinsic parameter of the filter. The exact choice of the kernel for the low-pass filter (here Heaviside functions in both wave numbers  $k_x$  and  $k_\theta$ ) matters little as long as the scale separation is sufficiently well pronounced. Consider the continuity equation in cylindrical coordinates :

$$\partial_x u_x + \frac{1}{r} \partial_r (r u_r) + \frac{1}{r} \partial_\theta u_\theta = 0. \quad (5)$$

The divergence operator commutes with  $\mathcal{L}$ , which leads to the same equation for the large-scale flow :

$$\partial_x U_x + \frac{1}{r} \partial_r (r U_r) + \frac{1}{r} \partial_\theta U_\theta = 0. \quad (6)$$

Multiplying Eq. (6) by  $r$  and integrating it from  $r = R_i$  to  $R_o$  leads to

$$\int_{R_i}^{R_o} \partial_\theta U_\theta dr = - \int_{R_i}^{R_o} \partial_x U_x r dr. \quad (7)$$

We now define radial integration

$$\overline{(\cdot)} = \frac{\int_{R_i}^{R_o} r(\cdot) dr}{\int_{R_i}^{R_o} r dr}. \quad (8)$$

Since  $\overline{U_x}$  does not vanish, then we can define an angle  $\alpha \geq 0$  with respect to the streamwise direction by

$$\tan \alpha(x, \theta, t) = \left| \frac{\overline{U_\theta(x, \theta, t)}}{\overline{U_x(x, \theta, t)}} \right|. \quad (9)$$

## 4.2 Spectral analysis

In order to evaluate which large-scale components are present here, time-averaged pre-multiplied energy spectra evaluated at gap center are shown in Fig. 10 for  $\text{Re}_\tau = 56$  (for which all flows are spatially intermittent) and for different values of  $\eta$  from 0.1 to 0.8. Energy spectra are based on the two-dimensional Fourier transform  $\widehat{u}_i(k_x, y, k_z)$  of  $u'_i(x, y, z)$  with respect to  $x$  and  $z$ , for all  $y$ . The streamwise one-dimensional spectra associated with the streamwise and azimuthal velocity fluctuations  $u'_x$  and  $u'_\theta$  are defined respectively by

$$E_{xx}(k_x, y) = \frac{L_x L_z}{(2\pi)^2 T} \int_t^{t+T} \int_0^\infty \Re(\widehat{u}_x \widehat{u}_x^*) dk_z dt, \quad E_{\theta\theta}(k_x, y) = \frac{L_x L_z}{(2\pi)^2 T} \int_t^{t+T} \int_0^\infty \Re(\widehat{u}_\theta \widehat{u}_\theta^*) dk_z dt. \quad (10)$$

The asterisk represents complex conjugation,  $T$  is the averaging time, and  $\Re$  denotes the real part. The proportionality constant is chosen so that

$$\int E_{xx}(k_x) dk_x = \int E_{xx}(k_z) dk_z = \langle u'_x u'_x \rangle, \quad \int E_{\theta\theta}(k_x) dk_x = \int E_{\theta\theta}(k_z) dk_z = \langle u'_\theta u'_\theta \rangle \quad (11)$$



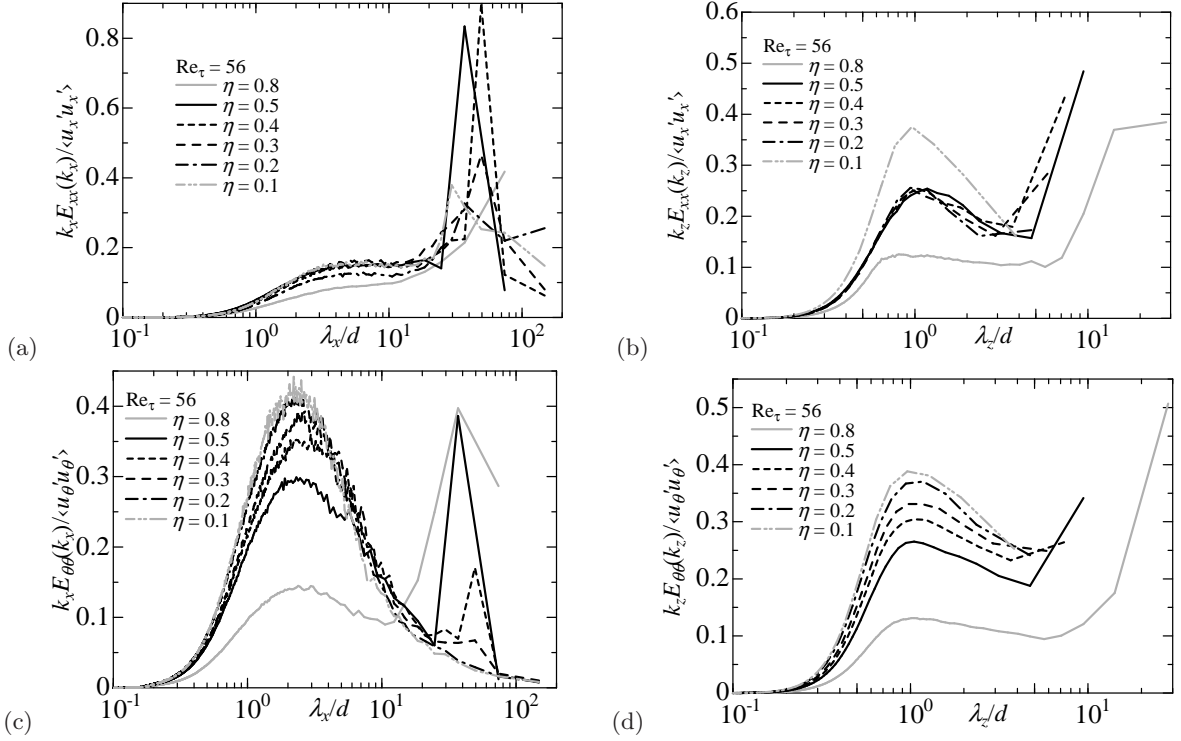


FIG. 10. Pre-multiplied energy spectra for  $u'_x$  and  $u'_\theta$  as a function of either wavelength  $\lambda_x/d$  or  $\lambda_z/d$  at mid-gap : (a) streamwise spectra of  $u'_x$ , (b) spanwise spectra of  $u'_x$ , (c) streamwise spectra of  $u'_\theta$ , and (d) spanwise spectra of  $u'_\theta$ . The streamwise and azimuthal wavenumbers are defined as  $k_x = 2\pi/\lambda_x$  and  $k_z = 2\pi/\lambda_z$ , respectively. The spectra are normalized by an ensemble-averaged value of  $u'_i u'_i$  at mid-gap.

as function of either  $k_x$  or  $k_\theta$ , where averaging  $\langle \cdot \rangle$  is performed over  $x$ ,  $\theta$ , and  $t$ .

Careful analysis of Fig. 10 reveals robust features. Small scales associated with turbulent fluctuations are present around  $\lambda_x/d \approx 2-3$  and  $\lambda_z/d \approx 1$  in all directions for all components. The situation is different for large-scale velocity components : out of the four figures in Fig. 10, only  $u_x$  as a function of  $x$  displays large scales for all value of  $\eta$ . These large scales do not appear strongly separated from the smaller ones, and are located at  $\lambda_x/d \approx 15-70$ . Neither  $u_\theta$  as a function of either  $x$  or  $\theta$ , nor  $u_x$  as a function of  $\theta$ , possesses such a robust large-scale component. Only as  $\eta$  exceeds 0.3, do well-separated peaks at similar large scales emerge in each spectrum. Important information can be deduced from these spectra. First, should large scales be found, the corresponding cut-off can be located safely in the intervals  $\lambda_x^c/d \approx 10-20$  and  $\lambda_z^c/d \approx 2-5$ . Secondly, by construction the wavelengths in the spectra are limited by the box dimensions  $L_x$  and  $L_z$ . A clear difference emerges between Figs. 10(a, c) on one hand (showing the  $\lambda_x$  dependence), and Figs. 10(b, d) on the other hand (showing the  $\lambda_z$  dependence) : in the latter case the occurrence of an azimuthal large-scale peak for both  $x$  and  $\theta$  components is ruled out when  $L_z \ll \lambda_z^c$ . In other words, the spanwise large-scale component is present only for sufficient azimuthal extent, whereas streamwise large-scale modulations are always present as long as the flow features spatial intermittency. We emphasize here that the azimuthal extent should be measured in units of  $d = R_o - R_i$ , since streaks and streamwise vortices (forming the small scales) scale with the gap size  $d$  rather than with any of the two radii  $R_o$  or  $R_i$ . Wall units are another candidate, but large-scale structures of interest are generally considered to scale with outer units. Our hypothesis here is that the occurrence of azimuthal large-scale flows depends directly on the azimuthal extent  $L_z/d$ , itself a function of  $\eta$ .

The quantity  $L_z$ , however, depends on the value of  $r$ . It is simpler to focus on the inner and outer azimuthal extents  $L_{zi}$  and  $L_{zo}$ , given respectively by

$$L_{zi} = 2\pi d \frac{\eta}{1-\eta} \quad (12)$$

$$L_{zo} = 2\pi d \frac{1}{1-\eta}. \quad (13)$$

Both quantities (expressed in units of  $d$ ) are plotted as functions of the radius ratio  $\eta$  in Fig. 11.

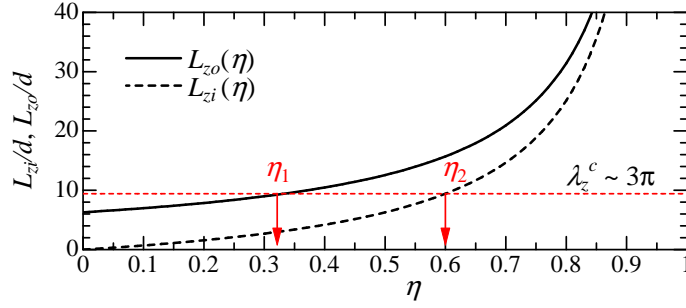


FIG. 11. Azimuthal length as a function of radius ratio.

Let us fix rather arbitrarily a cut-off value  $\lambda_z^c$ . The intersection of the horizontal line  $L_z = \lambda_z^c$  with the curves  $L_{zo}(\eta)$  and  $L_{zi}(\eta)$  in Fig. 11 defines two values of  $\eta$ , respectively  $\eta_1$  and  $\eta_2$ . This leads to three distinct ranges of values for  $\eta$  :

- for  $0 < \eta \leq \eta_1$ , there is no space for large scales in the azimuthal direction, neither at the inner nor at the outer wall. As a consequence  $\overline{U_\theta} = 0$  for all  $r$ , and  $\partial_x \overline{U_x} = 0$ .
- for  $\eta_2 \leq \eta \leq 1$ , azimuthal large scales can form at both inner and outer walls :  $\partial_\theta \overline{U_\theta} = -\partial_x \overline{U_x}$  with  $\overline{U_\theta} \neq 0$ . The situation is then analogous to the planar case.
- for  $\eta_1 \leq \eta \leq \eta_2$ , the situation is mixed : azimuthal large scale flows cannot be accommodated at all locations in the cross-section. A probabilistic approach is required.

For instance, choosing  $\lambda_z^c/d = 3\pi$  leads to  $\eta_1 = 1/3$  and  $\eta_2 = 3/5$ , which is consistent with our observations. While the classification above is not useful in practice to predict accurately the transition thresholds  $\eta_1$  and  $\eta_2$  (mainly because of the difficulty to define a unique cut-off value  $\lambda_z^c(\text{Re}_\tau)$ ), it captures the main physical idea : the presence of confinement in the azimuthal direction defines the two extreme regimes of straight interfaces (associated with puffs) or oblique interfaces (associated with oblique stripes). In addition, there is a range of value of  $\eta$  for which there is a probability of observing both types of interfaces (and hence both puffs and stripes) in the same flow at different times and/or different positions.

It can be useful to investigate cross-sections of the flow in the different regime to understand the implications of the previous hypothesis. The two-dimensional contours of  $u'_x$  and  $u'_\theta$  in arbitrary chosen  $(r-\theta)$  cross-sections are shown in Figs. 12 and 13, respectively, for different values of  $\eta$ .

The isocontours of  $u'_x$  in Fig. 12 allow one to count the numbers of streaks present in the vicinity of each wall. Each of these streaks has a radial and azimuthal extent  $\approx d/2$ , and the analysis of the spectra in Fig. 10 also suggests that their streamwise extent is approximatively  $2d$ . In principle one would expect the streak size to scale in inner units  $\nu/u_\tau$ , however the range of values of  $\text{Re}_\tau$  investigated here is relatively narrow and we prefer to report the dimensions of the streaks in (outer) units of  $d$ , as the relation  $\lambda_z \approx d$  emphasizes their quasi-circular cross-section. In the case of the straight puffs found for  $\eta = 0.1$ ,  $u'_x$  shows no large-scale azimuthal modulation, while high-order modulations (streaks) can be easily noted. With increasing  $\eta$ , the number of streaks increases as the azimuthal extent increases, a supplementary confirmation that the relevant lengthscale here is  $d$  rather than  $R_o$  or  $R_i$ . For  $\eta = 0.5$  and  $0.8$  (Fig. 12(d, e)), the low-order non-axisymmetric modulation of  $u'_x$  is the direct signature of the helix-shaped turbulence. To a lesser degree, such a modulation can also be visually detected for  $\eta = 0.2$  and  $0.3$  (Fig. 12(b, c)). Similar conclusions can be drawn from the isocontours of  $u'_\theta$  in Fig. 13 as well.

### 4.3 Statistics of transverse large-scale flows

This section is now devoted to a quantitative investigation of the orientation of the large-scale flow near the interfaces for varying radius ratio  $\eta$ . We begin by describing in more detail how data from the previous direct numerical simulations is post-processed. Based on the apparent scale separation in the spectra from Fig. 10, we

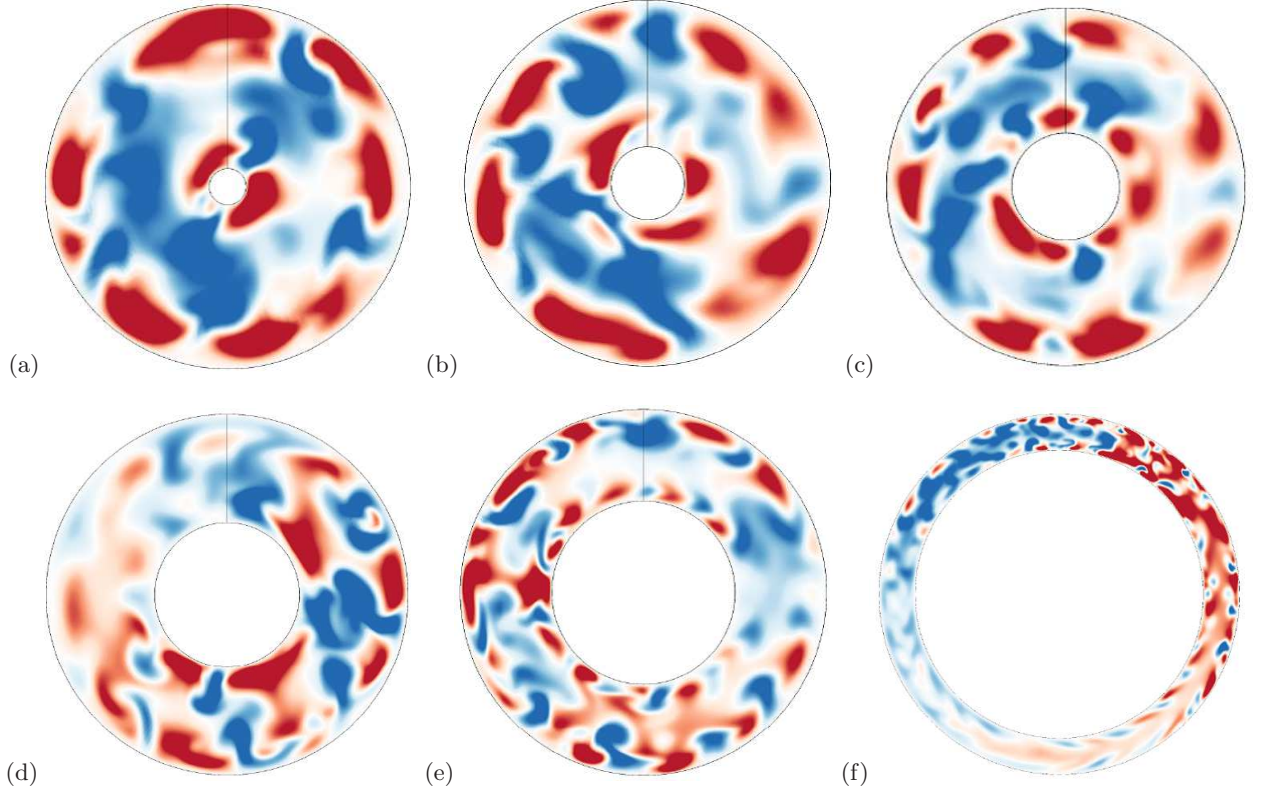


FIG. 12. Two-dimensional cross-sections  $(r, \theta)$  of instantaneous  $u'_x$  for  $\eta =$  (a) 0.1, (b) 0.2, (c) 0.3, (d) 0.4, (e) 0.5, and (f) 0.8 at  $\text{Re}_\tau = 52$ . Colourmap from  $-3.0u_\tau$  (blue) to  $+3.0u_\tau$  (red).

consider a low-pass filter  $\mathcal{L}$  whose kernel in spectral  $(k_x, k_z)$  space reads

$$|k_x| \leq \frac{2\pi}{20d}, \quad |k_z| \leq \frac{2\pi}{2d} \quad (14)$$

The original velocity fields  $\mathbf{u}(x, r, \theta, t)$  are transformed via  $\mathcal{L}$  into filtered fields  $\mathbf{U}(x, r, \theta, t)$ . The two-dimensional wall-integrated large-scale flow  $(\overline{U}_x, \overline{U}_\theta)$  is then computed using the definitions in Eq. (8).

An instantaneous snapshot of the large-scale flow  $\mathbf{U}(x, r, \theta, t)$  is plotted for several values of  $r$  together with its wall-integrated counterpart, namely,  $\overline{U}_x(x, \theta, t)$  and  $\overline{U}_\theta(x, \theta, t)$ . The cases  $\eta = 0.5$  and  $\eta = 0.1$  are respectively shown in Figs. 14 and 15. These plots highlight the genuinely three-dimensional structure of the velocity field  $\mathbf{U}$ . For  $\eta = 0.5$ , where turbulence clearly takes a helical shape, it can be verified that the local orientation of  $\mathbf{U}$  does not necessarily match that of the laminar-turbulent interface. The two-dimensional counterpart  $(\overline{U}_x, \overline{U}_\theta)$  however does point in a direction parallel to the interface, which confirms the previous hypothesis about the role of the large-scale flows. The situation is less clear in the puff case in Fig. 15. Unlike for higher  $\eta$  no robust oblique large-scale flow can be found, neither on arbitrary- $r$  cylinders nor for the wall-integrated field  $(\overline{U}_x, \overline{U}_\theta)$ .

Let us focus also on the local angle  $\alpha$  of the large-scale flow defined by Eq. (9), in addition to the azimuthal velocity component  $\overline{U}_\theta$  alone. Both quantities are functions of  $(x, \theta)$  position and time. Statistics of  $\overline{U}_\theta$  and  $\alpha$  have been gathered for all parameters over the numerical grid  $(x_i, z_j)$  and over different times. Since we are mainly interested in the values of  $\overline{U}_\theta$  at the laminar-turbulent interfaces, we exclude from the statistics fully laminar portions of the flow which would overestimate the statistical weight of the  $\overline{U}_\theta \approx 0$  contribution. This is achieved by conditioning all statistics by the additional constraint  $|u'_r|/u_\tau > 0.2$  (which is never fulfilled in laminar zones where  $u'_r \approx 0$ ). Probability distribution functions (PDFs) for  $|\overline{U}_\theta|$  and  $\alpha$  are obtained by considering bins of width  $\Delta\overline{U}_\theta = 0.025$  and  $\Delta\alpha = 0.25$ .

We first describe the PDFs of  $|\overline{U}_\theta|$  (normalised by  $u_\tau$ ) obtained for several values of  $\eta$  and parametrised by  $\text{Re}_\tau$ , and shown in Fig. 16(a). For  $\eta = 0.1, 0.2$  and  $0.3$ , the PDF looks reasonably Gaussian. This excludes statistically

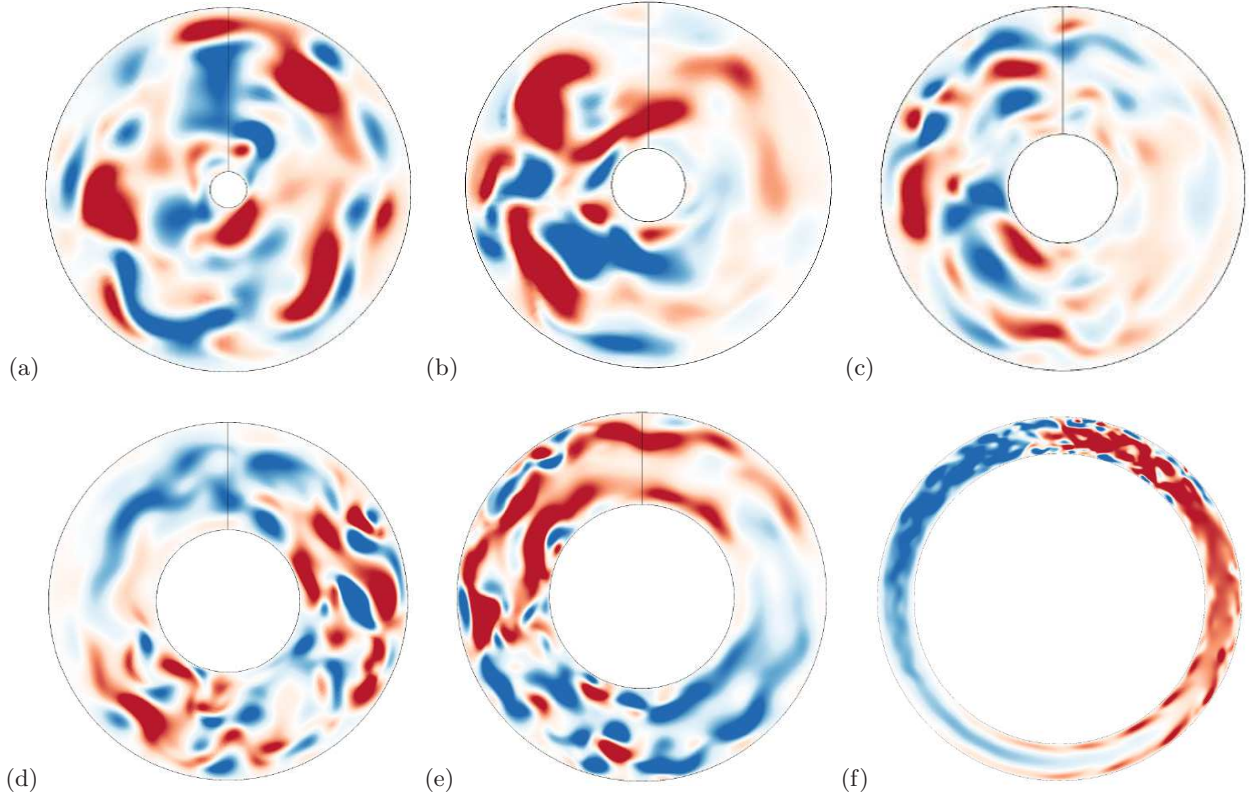


FIG. 13. Two-dimensional cross-sections  $(r, \theta)$  of instantaneous  $ru'_\theta$  for  $\eta =$  (a) 0.1, (b) 0.2, (c) 0.3, (d) 0.4, (e) 0.5, and (f) 0.8 at  $\text{Re}_\tau = 52$ . Colourmap from  $-1.0u_\tau$  (blue) to  $+1.0u_\tau$  (red): the positive direction of  $\theta$  is clockwise in the plots.

significant non-zero values of the azimuthal component. Note that we are here only considering the radially-integrated azimuthal large-scale velocity component, which in principle does not exclude local weak 'zonal' flows [21] with an almost vanishing radial average. For increasing values of  $\eta \geq 0.3$ , the tendency for the PDF to flatten away from zero becomes stronger, thereby enlarging the range of values of  $|\overline{U_\theta}|$ . For  $\eta = 0.4$ , a new peak emerges in the PDF from the former tail in the range  $\overline{U_\theta} = 0.2-0.3u_\tau$ , and this peak overweighs clearly the  $\overline{U_\theta} = 0$  contribution at  $\eta \geq 0.5$ . This shows how increasing  $\eta$  beyond 0.3 leads with increasing probability to the emergence of a transverse large-scale flow component, interpreted as responsible for the oblique interfaces observed. Focusing on the lowest values of  $\text{Re}_\tau = 52$  and 56 where intermittency has been observed, we next analyse more quantitatively the PDFs of both  $|\overline{U_\theta}|/u_\tau$  and  $\alpha$ , parametrised by  $\eta$  in the range 0.1–0.8, cf. Figs. 16(a, b), with the aim of extracting a comprehensive bifurcation diagram as a function of  $\eta$ .

The transition from a unimodal distribution of both (unsigned)  $\overline{U_\theta}$  and  $\alpha$  cannot be well analysed using standard statistical moments such as the mean and the variance. Instead we can extract, for both distributions, the statistical mode  $M$ , i.e. the global maximum of each PDF. They are reported in Fig. 17(a) and 17(b), respectively. In both cases the maximum is at 0 for  $\eta \leq 0.3$  and jumps to a non-zero value for the next investigated value, i.e. for  $\eta \geq 0.4$ . The mode initially increases as  $\eta$  increases, however we note a decrease of both  $M(\overline{U_\theta}/u_\tau)$  and  $M(\alpha)$  for the largest value of  $\eta = 0.8$ . This is due to the flattening of the PDF observed in Fig. 16 due to a wider range of possible angles (not shown). The statistical mode analysis allows to read directly the typical angles of the oblique stripes of Fig. 17(b). However, it does not yield an accurate value of the critical value  $\eta_c(\text{Re}_\tau)$  of  $\eta$  at which stripes emerge : all that can be deduced is that  $\eta_c$  lies in the range  $[0.3 : 0.4]$ . An alternative, specific to the case of unimodal-bimodal transitions, is to measure the convexity of the PDF near the origin. Suppose that the PDFs in Fig. 16 are even functions  $p(x)$  and can be fitted near the origin  $x = 0$  as

$$p(x, \eta, \text{Re}_\tau) = ax^2 + c, \quad (15)$$

with  $a = a(\eta, \text{Re}_\tau)$  and  $c = p(0, \eta, \text{Re}_\tau)$ . The coefficient  $a(\eta, \text{Re}_\tau)$  is negative for a unimodal distribution centred at  $x = 0$  and positive for a bimodal distribution whose maximum lies away from  $x = 0$ . As a consequence,  $a(\eta, \text{Re}_\tau) = 0$  can be used to define  $\eta_c(\text{Re}_\tau)$ . The values of  $a(\eta, \text{Re}_\tau)$  are plotted in Fig. 18 as functions of  $\eta$  parametrised by  $\text{Re}_\tau$

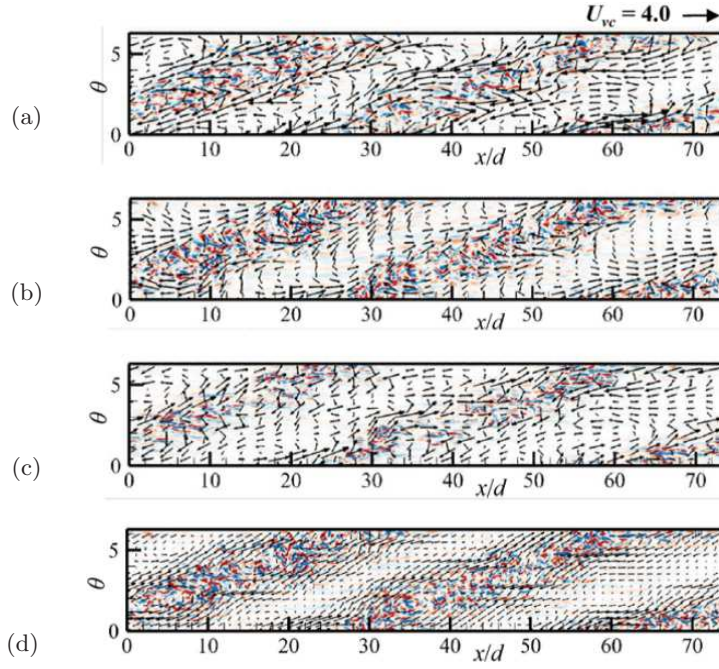


FIG. 14. Two-dimensional contours of instantaneous  $u'_r$  (blue, red)  $= (-1.0, 1.0)$  and large-scale flow  $(U_x, rU_\theta)$  as vectors at  $y/d =$  (a) 0.19, (b) 0.5, and (c) 0.81, for  $\eta = 0.5$  and  $\text{Re}_\tau = 56$ . Wall-normal-averaged large-scale flow  $(\overline{U}_x, \overline{U}_\theta)$  with contours of  $u'_r$  at mid-gap is shown in (d). The reference-vector length  $U_{VC}$  is shown in the top right of (a).

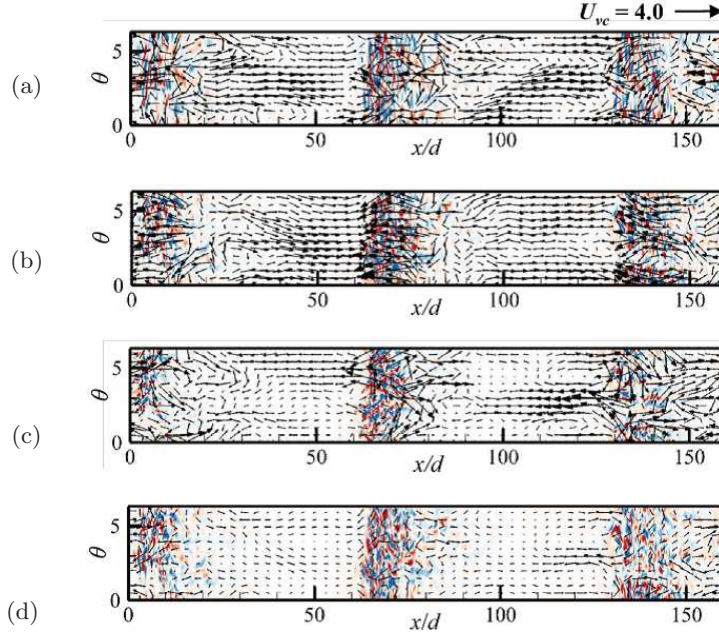


FIG. 15. Same as Fig. 14, but at  $y/d =$  (a) 0.25, (b) 0.5, and (c) 0.75, for  $\eta = 0.1$  and  $\text{Re}_\tau = 56$ .

after the PDF of  $\alpha$  has been approximated by a quadratic function using a least squares algorithm. Consistently with the mode analysis,  $\eta_c$  lies in the interval  $[0.3 : 0.4]$  for both  $\text{Re}_\tau = 64$  and  $56$  (the value  $\text{Re}_\tau = 80$  has been omitted as it is too high to sustain oblique stripes). The present data suggests even a slight decrease of  $\eta_c$  with  $\text{Re}_\tau$ , but this remains to be verified for a larger number of values of  $\text{Re}_\tau$ .

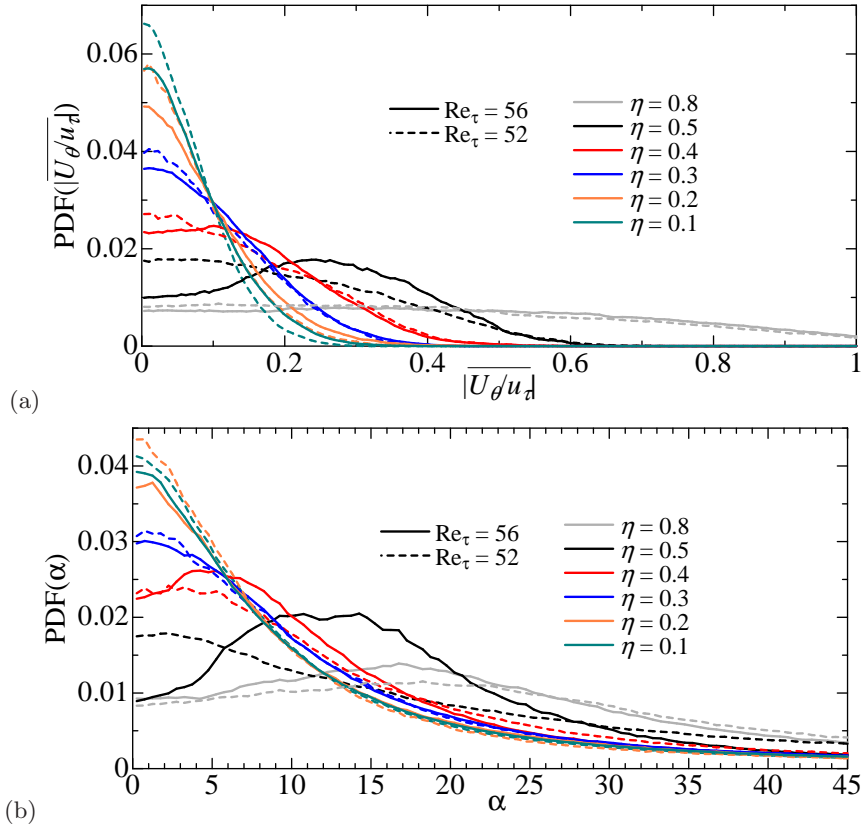


FIG. 16. PDFs of quantities that characterise the azimuthal large-scale flow and laminar-turbulent interface : (a)  $|\overline{U_\theta}|/u_\tau$  and (b)  $\alpha$ , for  $Re_\tau = 52$  and  $56$ ,  $\eta = 0.1-0.8$ .

## 5. DISCUSSION

The present results have confirmed that annular pipe flow (aPf), parametrised by both its radius ratio  $\eta$  and the friction Reynolds number  $Re_\tau$ , is a relevant candidate to track the transition from puffs to oblique stripes. The main physical mechanism responsible for this transition is the relaxation of the azimuthal confinement (measured in units of the gap  $d$ ) as  $\eta$  increases, allowing for more freedom in the orientation of the large-scale flow occurring at the laminar-turbulent interfaces, should such interfaces exist. Beyond a critical azimuthal extent, a neater selection of orientations occurs, ruled by the mass conservation at the interfaces. As  $\eta$  increases from 0 to 1, the following turbulent regimes are encountered :

- spatio-temporal intermittency as in circular pipe flow for  $0 < \eta \lesssim 0.2$
- mixed distribution of straight and helical puffs for  $0.2 \lesssim \eta \lesssim 0.4$
- regular patterns of oblique stripes, so-called helical turbulence, for  $\eta \gtrsim 0.5$
- disordered patterns of oblique stripes for  $0.5 \ll \eta \lesssim 1$ .

The last item has not been verified here but is expected to match all observations in extended planar shear flows (with additional effects due to the small wall curvature). This apparent disorganisation occurs when the transverse extent is sufficiently larger than the correlation length of the intermittent regime, at least sufficiently above the critical point  $Re_\tau^c(\eta)$ . The parameter space may also contain new regimes so far unexplored. A statistical analysis has been carried out by focusing entirely on the local structure and orientation of the large-scale flow. Note that other approaches are possible to handle bifurcations from one turbulent regime to another one. When the two regimes of interest are characterised by symmetry breaking (as is the case here where each oblique stripe violates the  $\overline{U_\theta} = 0$  symmetry), other order parameters can be considered (see e.g. [22]). In the spirit of pattern formation, the statistics of some well-chosen spectral coefficient characteristics of the structures under study can be helpful. The transition

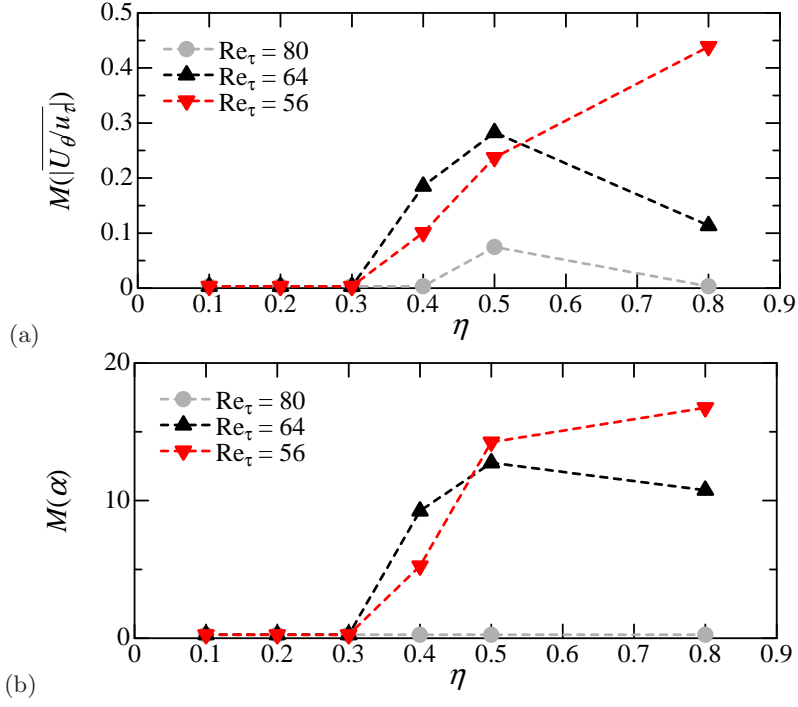


FIG. 17. Statistical mode extracted from the PDFs in Fig. 16 of : (a)  $|\overline{U_\theta}|/u_\tau$  and (b)  $\alpha$ , for  $Re_\tau = 52$  and  $56$ ,  $\eta = 0.1-0.8$ . The data suggests a critical value of  $\eta = \eta_c$  between 0.3 and 0.4.

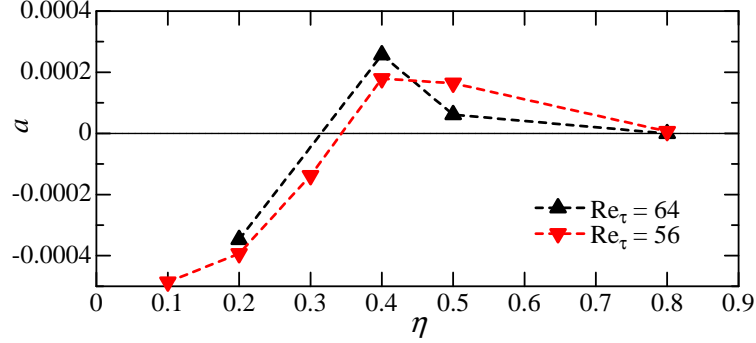


FIG. 18. Coefficient  $a$  in Eq. (15) extracted from the PDF of the angle  $\alpha$ .

from full turbulence to stripe patterns or to puffs has been considered precisely in this manner for various shear flows [16, 23, 24]. Orientation reversals of turbulent stripes in pCf were also monitored by considering the competition between two or more Fourier coefficients corresponding to different wavevectors [25]. Modal approaches however show the strong disadvantage of being domain-dependent. We believe that the current statistical approach, more local than modal, is more adapted to the spatio-temporally intermittent flow regimes encountered here, especially for low  $\eta$ .

While an experimental verification of such flow regimes is called for, it is instructive to discuss whether other shear flow geometries lend themselves easily to bifurcations between intermittently turbulent regimes. The transition from puffs to stripes corresponds essentially, as previously shown, to a transition from one-dimensional to two-dimensional coexistence, via the occurrence of quasi-one-dimensional stripe patterns. Other homotopies can be suggested by similarly tuning the confinement in the direction transverse to the mean flow. Imposing confinement by sidewalls in an otherwise Cartesian geometry is a possible option. A rectangular duct flow driven by a pressure gradient, with a cross-section of dimensions  $L_y \times L_z$ , can be parametrised both by a Reynolds number and an aspect ratio  $A = L_z/L_y$  ( $A \geq 1$  by convention). The geometry of  $A = 1$  corresponds to a square duct whereas  $A \rightarrow \infty$  is equivalent to plane

Poiseuille flow. The laminar profile is known to be linearly stable for all values of  $Re_\tau$  of interest here. This parametric problem has been considered numerically in Ref. [26]. Again straight puffs have been identified for  $A \leq 3$  whereas spots with somewhat oblique interfaces have been visualised for  $A \geq 4$ . The authors have reported a peculiarity of the confinement by solid sidewalls : permanent local relaminarisation at the sidewalls affecting the localisation of the turbulent structure. This is consistent with the recent experimental observations of spots in a duct flow with aspect ratio  $A = 7.5$  [27]. While this system has the advantage of dealing with flat walls only, the local relaminarisation at the sidewalls is interpreted as an additional complication obscuring the transition from puffs to oblique stripes.

Other examples closer to the present case of aPf share a common geometry but differ in the way energy is injected into the flow. The Taylor-Couette system, where the two coaxial cylinders rotate with different frequencies  $\Omega_i$  and  $\Omega_o$  in the absence of an axial pressure gradient, is such an example. It is known that for  $\eta \rightarrow 1$ , the case of exact counter-rotation  $\mu = \Omega_o/\Omega_i = -1$  corresponds to plane Couette flow, which has a linearly stable base flow. It has been experimentally verified for  $\eta$  slightly below 1 that low- $Re$  regimes with  $\mu \approx -1$  feature two-dimensional intermittent arrangements of oblique stripes with both positive and negative angles [6, 28, 29]. Reducing  $\eta$  with fixed  $\mu$ , however, leads to changes in the stability of the base flow. Other regimes such as those featuring interpenetrating spirals [30] enter the bifurcation diagram and make the continuation from stripes to puffs unlikely. It is an open question whether other paths in an enlarged parameter space could lead to such a transition.

Finally, an interesting candidate for the continuation from stripes to puffs is the sliding Couette flow (sCf), where the outer cylinder is fixed and the inner one moves axially with a constant velocity (see e.g. [31]). This flow is thought to be equivalent to pCf in the  $\eta \rightarrow 1$  limit and again to pipe flow in the vanishing  $\eta$  limit. It has been verified numerically [32] that this system bridges puffs to spots in a way apparently similar to the present system. Whether and how the homotopies in sCf and aPf really differ remains an open question. However, aPf shows the important advantage of being easier to achieve experimentally as it does not include any motion of the solid walls, only a pressure gradient imposed on a fixed geometry.

## Acknowledgements

T.I. was supported by a Grant-in-Aid from JSPS (Japan Society for the Promotion of Science) Fellowship #26-7477. This work was partially supported by JSPS KAKENHI Grant Number 16H06066 and 16H00813. The present simulations were performed on supercomputers at the Cyberscience Centre of Tohoku University and at the Cybermedia Centre of Osaka University. We thank JSPS, CNRS (Centre National de la Recherche Scientifique), and RIMS (Research Institute for Mathematical Sciences) for additional travel support.

- 
- [1] Paul Manneville, “Transition to turbulence in wall-bounded flows: Where do we stand?” *Mechanical Engineering Reviews* (2016).
  - [2] I. J. Wignanski and F. H. Champagne, “On transition in a pipe. Part 1. The origin of puffs and slugs and the flow in a turbulent slug,” *J. Fluid Mech.* **59**, 281–335 (1973).
  - [3] K. Avila, D. Moxey, A. de Lozar, M. Avila, D. Barkley, and B. Hof, “The onset of turbulence in pipe flow,” *Science* **333**, 192–196 (2011).
  - [4] Dwight Barkley, “Theoretical perspective on the route to turbulence in a pipe,” *Journal of Fluid Mechanics* **803** (2016).
  - [5] Jose Eduardo Wesfreid and Lukasz Klotz, “Subcritical transition to turbulence in Couette-Poiseuille flow,” *Bulletin of the American Physical Society* **61** (2016).
  - [6] A. Prigent, G. Grégoire, H. Chaté, O. Dauchot, and W. van Saarloos, “Large-scale finite-wavelength modulation within turbulent shear flows,” *Phys. Rev. Lett.* **89**, 014501 (2002).
  - [7] T. Tsukahara, Y. Seki, H. Kawamura, and D. Tochio, “DNS of turbulent channel flow at very low Reynolds numbers,” in *Proc. Fourth Int. Symp. on Turbulence and Shear Flow Phenomena*, edited by J. A. C. et al. Humphrey (Williamsburg, USA, 2005) pp. 935–940, arXiv preprint: 1406.0248.
  - [8] Y. Duguet, P. Schlatter, and D. S. Henningson, “Formation of turbulent patterns near the onset of transition in plane Couette flow,” *J. Fluid Mech.* **650**, 119–129 (2010).
  - [9] Grégoire Lemoult, Liang Shi, Kerstin Avila, Shreyas V Jalikop, Marc Avila, and Björn Hof, “Directed percolation phase transition to sustained turbulence in Couette flow,” *Nature Physics* (2016).
  - [10] D. Barkley, “Simplifying the complexity of pipe flow,” *Phys. Rev. E* **84**, 016309 (2011).
  - [11] J. E. Walker, G. A. Whan, and R. R. Rothfus, “Fluid friction in noncircular ducts,” *AIChE Journal* **3**, 484–489 (1957).
  - [12] C. J. Heaton, “Linear instability of annular Poiseuille flow,” *J. Fluid Mech.* **610**, 391–406 (2008).



- [13] Takahiro Ishida, Yohann Duguet, and Takahiro Tsukahara, “Transitional structures in annular Poiseuille flow depending on radius ratio,” *Journal of Fluid Mechanics* **794**, R2 (2016).
- [14] H. Abe, H. Kawamura, and Y. Matsuo, “Direct numerical simulation of a fully developed turbulent channel flow with respect to the Reynolds number dependence,” *J. Fluids Eng.* **123**, 382–393 (2001).
- [15] Jimmy Philip and Paul Manneville, “From temporal to spatiotemporal dynamics in transitional plane Couette flow,” *Physical Review E* **83**, 036308 (2011).
- [16] D. Moxey and D. Barkley, “Distinct large-scale turbulent-laminar states in transitional pipe flow,” *PNAS* **107**, 8091–8096 (2010).
- [17] M. Shimizu, P. Manneville, Y. Duguet, and G. Kawahara, “Splitting of a turbulent puff in pipe flow,” *Fluid Dyn. Res.* **46**, 061403 (2014).
- [18] X. Xiong, J. Tao, S. Chen, and L. Brandt, “Turbulent bands in plane-Poiseuille flow at moderate Reynolds numbers,” *Phys. Fluids*, 041702 (2015).
- [19] Y. Duguet and P. Schlatter, “Oblique laminar-turbulent interfaces in plane shear flows,” *Phys. Rev. Lett.* **110**, 034502 (2013).
- [20] James M Hamilton, John Kim, and Fabian Waleffe, “Regeneration mechanisms of near-wall turbulence structures,” *Journal of Fluid Mechanics* **287**, 317–348 (1995).
- [21] Nigel Goldenfeld and Hong-Yan Shih, “Turbulence as a problem in non-equilibrium statistical mechanics,” *Journal of Statistical Physics*, 1–20 (2016).
- [22] P-P Cortet, A Chiffaudel, F Daviaud, and B Dubrulle, “Experimental evidence of a phase transition in a closed turbulent flow,” *Physical Review Letters* **105**, 214501 (2010).
- [23] Laurette S Tuckerman, Dwight Barkley, and Olivier Dauchot, “Statistical analysis of the transition to turbulent-laminar banded patterns in plane Couette flow,” *Journal of Physics: Conference Series* **137**, 012029 (2008).
- [24] L. S. Tuckerman, T. Kreilos, H. Schrobdsorff, T. M. Schneider, and J. F. Gibson, “Turbulent-laminar patterns in plane Poiseuille flow,” *Phys. Fluids* **26**, 114103 (2014).
- [25] Joran Rolland and Paul Manneville, “Pattern fluctuations in transitional plane Couette flow,” *Journal of Statistical Physics* **142**, 577–591 (2011).
- [26] Keisuke Takeishi, Genta Kawahara, Hiroki Wakabayashi, Markus Uhlmann, and Alfredo Pinelli, “Localized turbulence structures in transitional rectangular-duct flow,” *Journal of Fluid Mechanics* **782**, 368–379 (2015).
- [27] Grégoire Lemoult, Konrad Gumowski, Jean-Luc Aider, and José Eduardo Wesfreid, “Turbulent spots in channel flow: An experimental study,” *The European Physical Journal E* **37**, 1–11 (2014).
- [28] Daniel Borrero-Echeverry, Michael F Schatz, and Randall Tagg, “Transient turbulence in Taylor-Couette flow,” *Physical Review E* **81**, 025301 (2010).
- [29] Kerstin Avila and Björn Hof, “High-precision Taylor-Couette experiment to study subcritical transitions and the role of boundary conditions and size effects,” *Review of Scientific Instruments* **84**, 065106 (2013).
- [30] C. David Andereck, S. S. Liu, and Harry L. Swinney, “Flow regimes in a circular Couette system with independently rotating cylinders,” *Journal of Fluid Mechanics* **164**, 155–183 (1986).
- [31] K. Deguchi and M. Nagata, “Bifurcations and instabilities in sliding Couette flow,” *Journal of Fluid Mechanics* **678**, 156–178 (2011).
- [32] Kohei Kunii, Takahiro Ishida, and Takahiro Tsukahara, “Helical turbulence and puff in transitional sliding Couette flow,” in *Proc. ICTAM 2016, Montréal, Canada* (IUTAM, 2016).